

Tunable Onset of Hydrogen Evolution in Graphene with Hot Electrons

Hyun Uk Chae, Ragib Ahsan, Jun Tao, Stephen B. Cronin, and Rehan Kapadia*

Cite This: *Nano Lett.* 2020, 20, 1791–1799

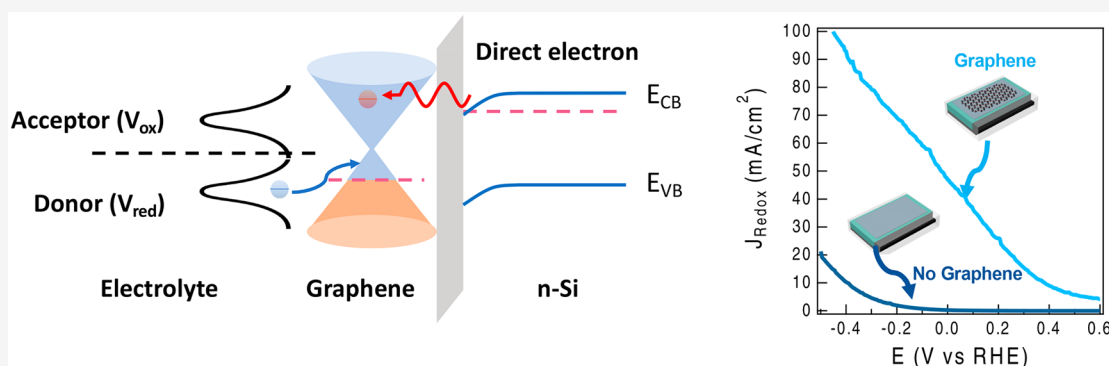
Read Online

ACCESS |

Metrics & More

Article Recommendations

Supporting Information



ABSTRACT: Here, we show that the turn-on voltage for the hydrogen evolution reaction on a graphene surface can be tuned in a semiconductor–insulator–graphene (SIG) device immersed in a solution. Specifically, it is shown that the hydrogen evolution reaction (HER) onset for the graphene can shift by >0.8 V by application of a voltage across a graphene– Al_2O_3 –silicon junction. We show that this shift occurs due to the creation of a hot electron population in graphene due to tunneling from the Si to graphene. Through control experiments, we show that the presence of the graphene is necessary for this behavior. By analyzing the silicon, graphene, and solution current components individually, we find an increase in the silicon current despite a fixed graphene–silicon voltage, corresponding to an increase in the HER current. This additional silicon current appears to directly drive the electrochemical reaction, without modifying the graphene current. We term this current “direct injection current” and hypothesize that this current occurs due to electrons injected from the silicon into graphene that drives the HER before any electron–electron scattering occurs in the graphene. To further determine whether hot electrons injected at different energies could explain the observed total solution current, the nonequilibrium electron dynamics was studied using a 2D ensemble Monte Carlo Boltzmann transport equation (MCBTE) solver. By rigorously considering the key scattering mechanisms, we show that the injected hot electrons can significantly increase the available electron flux at high energies. These results show that semiconductor–insulator–graphene devices are a platform which can tune the electrochemical reaction rate via multiple mechanisms.

KEYWORDS: Graphene, hot electron, direct injection, hydrogen generation, electron transfer, scattering mechanism

Electrocatalysis can be used to convert intermittent renewable energy generation into stored chemical energy.^{1–5} In general, these processes are an avenue toward creating fuels from abundant molecules. Thus, design of electrocatalysts is of significant interest. However, the primary focus of design efforts surrounds understanding and engineering the kinetic aspects of catalysts by increasing the density of active sites or the intrinsic activity of catalysts.^{6–10} In particular, graphene-based hot electron devices have been demonstrated to capture hot electrons generated by chemical reactions or photon absorption.^{11,12} Here, we show that, through controllable generation of hot electrons, we are able to electrically modulate the potential at which the HER occurs on monolayer graphene. This potentially introduces another avenue through which electrocatalysts may be engineered—through control over the electron distribution. Specifically, we

use a semiconductor–insulator–graphene (SIG) junction, whereby, when a voltage is applied, thermalized electrons from the semiconductor conduction band will tunnel across the insulator into the graphene, where they will initially be out of equilibrium with respect to the Fermi–Dirac distribution of the thermalized electrons in graphene. Regardless of the current limiting mechanism, it is important to highlight that all electrons injected from the silicon into the graphene will be

Received: December 5, 2019

Revised: February 24, 2020

Published: February 25, 2020

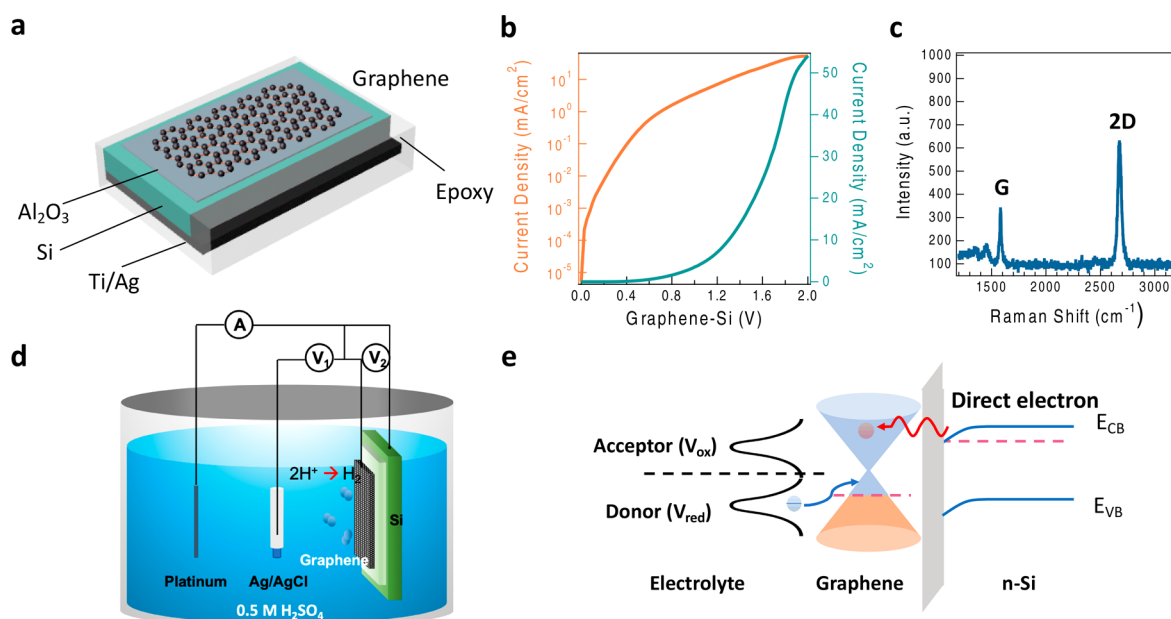


Figure 1. Device schematics, characterization, and hot electron transfer mechanism. (a) Schematic of the structure of the graphene–insulator–semiconductor device used here. (b) Current density vs applied voltage for the graphene/Al₂O₃/Si diode used here in both linear and log scale. (c) Raman spectroscopy of the graphene layer transferred on top of the Al₂O₃/Si substrate. (d) Electrochemical measurement setup for device characterization. (e) Band diagram of the device structure at the positively biased graphene–Si junction showing the injection of hot electrons.

hot electrons. Specifically, the thermal electrons in the silicon device will become hot electrons in the graphene after injection. If there were no other terminals in this device, those electrons would then cool to the graphene Fermi level, with the excess energy being dissipated as heat.¹³ However, in these devices, the graphene is also in contact with a solution, enabling electrons in the graphene to drive electrochemical reactions. Thus, depending on the relative rates of cooling and reaction, the injected hot electrons in graphene can traverse multiple pathways. We chose graphene due to the low electron–phonon coupling and electron density when compared to metals as well as the single layer physical structure.^{14,15} The lower electron scattering rates are important in reducing the hot electron cooling pathways, and the single layer structure enables every hot electron to be at the surface, maximizing the probability of driving electrochemical reactions. Recently, it was also shown that high quantum efficiency hot electron devices could be generated with thin films of gold, suggesting that a material such as graphene, which has superior properties from the perspective of hot electron devices, could perform better.¹⁶

In this work, we use a semiconductor–insulator–graphene junction to controllably create a hot electron population via tunneling of electrons from the semiconductor conduction band into the graphene layer and subsequently use the injected electron population to modulate the electrochemical reaction rate between the graphene and an aqueous solution. Figure 1a shows a schematic of the device structure which consists of a moderately doped n-type silicon wafer, an aluminum oxide insulator layer, and a graphene layer. The device is encapsulated with the epoxy to ensure only the graphene is in contact with the solution. After fabrication, we carried out dry I – V measurements to observe the diode behavior of the SIG device. Figure 1b shows both linear and log scale plots of the device I – V characteristic. As shown in the I – V curves, the diode shows two exponential regions, with different slopes,

which can be expected in a semiconductor–insulator–metal device, as the current may be limited by (i) injection over the silicon depletion region barrier, (ii) tunneling through the oxide, or (iii) parasitics. Here, the current appears to be limited by silicon injection between the voltage region of 0 and 0.4 V and then appears to be tunneling limited between 0.4 and 1.9 V. To ensure that the graphene was successfully transferred onto the device, we carried out Raman spectroscopy on multiple points on the device surface. A representative Raman spectrum of graphene on the aluminum oxide is shown in Figure 1c with sharp 2D and G peaks labeled at 2680 and 1580 cm⁻¹, respectively. The relative ratio of the measured I_{2D}/I_G peak intensity is ~ 2 , clearly identifying the monolayer graphene.¹⁷ The electrochemical measurement of this device was conducted by submerging it into the 0.5 M H₂SO₄, which acts as the collector of hot electrons in this device. A potentiostat with two independent channels is used for modulating (i) a graphene–solution junction voltage ($V_{\text{graphene-solution}}$) to control the electrochemical reaction and (ii) a graphene–silicon voltage ($V_{\text{graphene-Si}}$) to control the injection of high energy electrons from the silicon conduction band into the graphene. The schematic of the device measurement setup is shown in the Figure 1c. To understand the measurement setup, details are presented in Figure S1 in the Supporting Information. A schematic of the device and electrolyte band structure is shown in Figure 1e. One unique feature of this graphene-based device arises due to the small quantum capacitance of the graphene, allowing the Fermi level in the graphene to change as a function of graphene–Si junction bias.

To study the redox behavior of graphene devices, we carried out two types of I_{solution} measurements. The measured potentials here are rescaled to the RHE by using the equation $E_{\text{RHE}} = E_{\text{Ag/AgCl}} + 0.197 \text{ V} + 0.0592 \text{ V} \times \text{pH}$. First, we carry our linear sweep voltammetry (LSV) of the graphene–solution ($V_{\text{graphene-solution}}$) junction while simultaneously stepping the

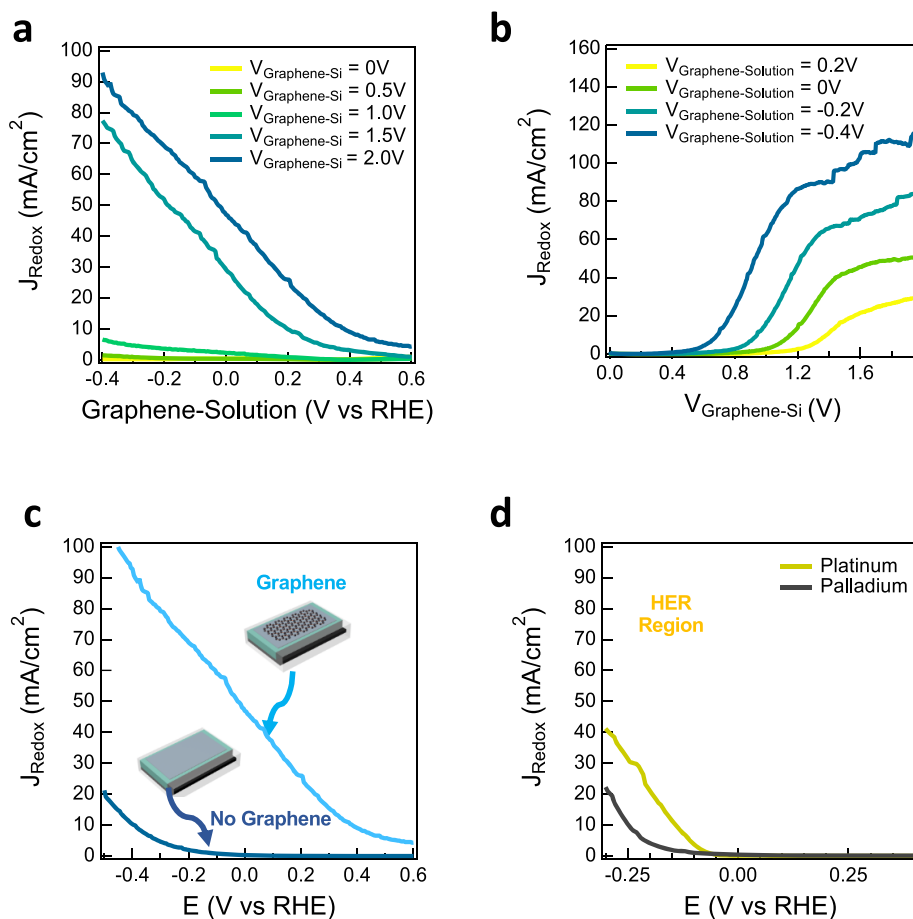


Figure 2. Linear sweep voltammetry (LSV) curves of the graphene SIG device and comparison devices. (a) Linear scale solution current density vs applied graphene–solution voltage for varying graphene–Si diode voltages and (b) solution current density vs applied graphene–Si voltage for stepping graphene–solution voltages. (c) Solution current density comparison with the no-graphene device. (d) Solution current density of Pt and Pd at the same scale of current density.

voltage of the graphene–silicon ($V_{\text{graphene-Si}}$) junction from 0 to 2 V with 0.5 V steps. Figure 2a shows the plots of the LSV. As the voltage between the graphene–silicon junction increases, the turn-on voltage for HER is reduced, and the current density at a given applied voltage increases. Particularly interesting are the cases of $V_{\text{graphene-Si}} = 1.5$ and 2.0 V. We see dramatic increases in the current, with the largest currents observed $> \sim 100$ mA/cm². Figure 2b on the other hand shows the plot of LSV of the graphene–silicon voltage while stepping with a fixed voltage across the graphene–solution junction. There are two key factors that determine whether an electron will be elastically transferred from graphene to a redox state, resulting in the observed solution redox current: (i) the probability of redox states at the given energy being available and (ii) the probability that the electron will be able to tunnel through the energy barrier posed by the electrochemical double layer at the graphene–solution interface. There is an activation energy barrier (ΔG_{act}) associated with the electron transfer, and the probability that an electron can overcome this barrier is dictated by thermal fluctuations.^{18,19} The probability of an electron being transferred into a redox state inside the solution quantitatively differs from that of being transferred into an adsorbed intermediate. According to the Anderson–Newns model of chemisorption on metal,²⁰ the density of states of an adsorbed atom will be shifted in energy as well as broadened. This density of states is proportional to the

electron transfer probability. According to this model, both the energy shift and broadening will have a complicated dependence on energy. Ignoring the energy dependence of the shift and broadening, the density of states takes the form of a Lorentzian distribution. A full study of such density of states requires considering the orbitals of the adsorbed atom and the orbitals of the adsorbent. However, for electron transfer to redox states inside the solution, the electron transfer probability and redox density of states are different and can be obtained from Gerischer’s model.²¹ According to this model, if an electron in graphene has an energy ΔE in excess to the energy of the redox state, the electron transfer probability is given by the Boltzmann term, $e^{-|\Delta G_{\text{act}} - \Delta E|/k_{\text{B}}T}$, where k_{B} is the Boltzmann constant.²² Within the harmonic oscillator approximation, this probability distribution takes the Gaussian form

$$W_{\text{O}}(\lambda, \Delta E, V_{\text{graphene-solution}}) = (4\pi\lambda k_{\text{B}}T)^{-1/2} \exp\left[-\frac{(\Delta E - \lambda - eV_{\text{graphene-solution}})^2}{4\lambda k_{\text{B}}T}\right] \quad (1)$$

Here, $\lambda = 4\Delta G_{\text{act}}^0$ is the reorganization energy of electron transfer, where ΔG_{act}^0 is the activation energy for $\Delta E = 0$ and $V_{\text{graphene-solution}} = 0$. The term $(4\pi\lambda k_{\text{B}}T)^{-1/2}$ normalizes the

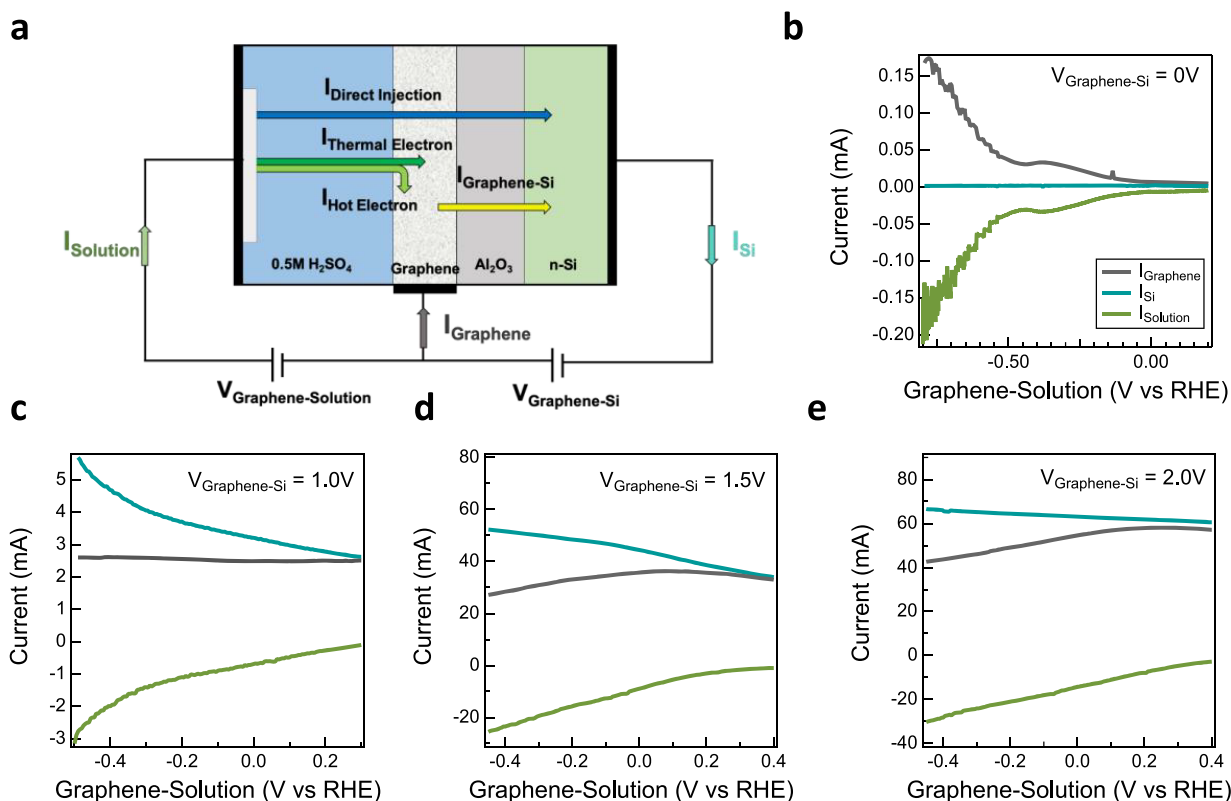


Figure 3. Composition of current inside the device and system and measurement results. (a) Schematic of current components flowing inside the system. Major currents (i.e., I_{Si} , $I_{graphene}$, and $I_{Solution}$) are composed of different minor current components. (b–e) Measurement of three major currents of the closed system, under different graphene–Si voltages.

distribution. Since the redox reaction happens at both redox species inside the solution and adsorbed to the electrode, ideally, the electron transfer probability should follow a combination of both the Lorentzian and Gaussian distribution. However, since we are more interested in understanding the physical phenomena and not performing a rigorous quantitative analysis, we can roughly approximate the Lorentzian distribution to a Gaussian distribution. This way, we can use the Gerischer model as a proxy to the more involved Anderson–Newns model for the sake of simplicity.

The probability that the electron can tunnel through the double layer barrier depends on the specifics of the double layer structure itself.¹⁸ To a first approximation, this probability should continuously increase with increasingly negative $V_{graphene-solution}$. When we approach more negative $V_{graphene-solution}$, W_0 follows the Gaussian distribution and increases in the beginning. Since typically λ takes a value between 1 and 3 eV, electron transfer probability will increase within the $V_{graphene-solution}$ range of our concern (0.2 to -0.4 V).¹⁸ In addition, tunneling probability also increases. Increases in both of these probabilities manifest themselves as an increased amount of current for increasingly negative $V_{graphene-solution}$. When $V_{Graphene-Si}$ becomes more positive, the injection current as well as the energy of the injected electron with respect to the graphene Dirac point increases. This high energy electron follows one of three pathways: (i) losing energy to other low energy electrons in graphene via electron–electron (e–e) scattering, (ii) losing energy to the lattice through phonon scattering, or (iii) transferring itself to the redox state and performing reduction of the H⁺ ion. In the steady state, this injection flux of electrons results in a

distribution of electrons differing from the Fermi distribution that have considerably higher energy compared to the thermal electrons. These hot electrons with energy $\Delta E = E - E_{redox}$ (E = energy of electron compared to Dirac point, E_{redox} = energy of standard redox state compared to Dirac point) will have a higher electron transfer probability as $\Delta E - \lambda - eV_{graphene-solution} \rightarrow 0$ limit. For an injection energy exceeding λ or $V_{graphene-solution} < -\lambda/e$, the electron transfer probability will start decreasing, whereas the tunneling probability should increase. However, the highest value tunneling probability can attain is 1 and therefore the Gaussian distribution will be the limiting factor in determining the success of an electron transfer.

To compare and analyze the source of these results, we carried out an identical experiment with the device which does not have graphene on top of the insulator layer. Figure 2c shows the solution current density vs graphene–solution voltage. Comparing the same amount of voltage, $V_{WE-Si} = 2$ V biased condition, which the working electrode represents graphene for the first device and aluminum oxide for the second device, the no-graphene device shows less current with ~ 5 mA/cm² at potential (V vs RHE) = -0.3 V, while the graphene device shows ~ 80 mA/cm², for which the relative ratio is ~ 18 . In addition, we measured the HER in the same electrolyte by using both the platinum and palladium electrodes, which are excellent electrocatalysts due to their near ideal positions on the volcano plots.^{23–25} Figure 2d shows the measured current density of platinum and palladium electrodes evaporated on top of the insulator layer as well. At $V_{graphene-Si} = 2.0$ V, the current density is ~ 2 and ~ 4 times higher than the platinum and palladium, respectively. It is

noteworthy that none of the previous works have presented a higher value than platinum in both turn-on voltage and current density at the same voltage vs the reference electrode. To eliminate the possibility of the effect of a lateral voltage drop in graphene, we measured two different samples with different ring electrode shapes and show that both devices demonstrate nearly identical current densities (Figure S2). We also carried out the same measurement in different types of electrolytes to verify the stability of our graphene device. Figure S4 shows the results of the cyclic voltammetry in the 1 mM ferrocene + 1 M KCl solution. The hot electron effect of the device can be distinguished from the tail of the graph at $V_{\text{graphene-Si}} = 1.5$ V. Figure S3 also shows the results of the LSV under alkaline conditions by using the 0.1 M KOH instead of the 0.5 M H_2SO_4 . These devices also show a similar hot electron effect in 0.1 M KOH solutions as well but with lower current. The reason the current level is reduced comes from the reduced availability of H^+ ions as well as different mechanisms of the HER in the different pHs of the electrolyte.²⁶ After the electrochemical measurements, to ensure the physical stability of our device, we carried out Raman spectroscopy to ensure that the graphene layer was still present. Figure S4 shows the eight points of Raman spectroscopy results showing 2D and G peaks all labeled at 2680 and 1580 cm^{-1} , respectively. The relative ratio of the measured $I_{2\text{D}}/I_{\text{G}}$ peak intensity here is still around 2; it is feasible to say that our device is stable even after several experimental runs.

Next, we analyze the current components that allow the graphene to have high currents by studying each of the three measured current components (I_{solution} , I_{graphene} , I_{Si}) from the potentiostat system. Figure 3a shows the schematic of the measured current components and the internal current components which compose them. The source of hot electrons in the graphene is the injection of electrons from the silicon conduction band tunneling through the oxide layer. In our measurement, the total redox current is measured through the I_{solution} current component. The platinum counter electrode is shared by two working electrodes (graphene and silicon); the total current can be measured by collecting all of the current components flow into the Pt counter electrode. The electrochemical reduction current on the graphene is separated into three components, reduction due to the thermal electron population of graphene itself, $I_{\text{thermal electron}}$, reduction due to the hot electron population, $I_{\text{hot electron}}$, and a direct electrochemical reduction component from the silicon to the solution, $I_{\text{direct injection}}$, which is the most significant factor in this work. These correspond to the measured components from the following relationships.

$$I_{\text{solution}} = -(I_{\text{graphene}} + I_{\text{silicon}}) \quad (2)$$

$$I_{\text{Graphene}} = I_{\text{thermal electron}} + I_{\text{hot electron}} - I_{\text{graphene-Si}} \quad (3)$$

$$I_{\text{Si}} = I_{\text{graphene-Si}} + I_{\text{direct injection}} \quad (4)$$

From these relationships, we can see that, when $V_{\text{graphene-Si}} = 0$ V, $I_{\text{graphene-Si}} = 0$ A, since none of the electrons are tunneling from the silicon conduction band. This shows the traditional three-electrode measurement where the graphene is the working electrode, and all of the total solution component comes from thermal electrons of graphene, which refers to $I_{\text{solution}} = -I_{\text{graphene}}$ in Figure 3b. Unlike other metal electrodes, the amount of thermal electrons from graphene is less due to the low density of states. Figure 3c–f shows the three

measured current components during a $V_{\text{graphene-solution}}$ linear voltage sweep for $V_{\text{graphene-Si}}$ from 0.5 to 2.0 V. Since the voltage between the graphene and silicon is fixed, the current injected from the silicon into the graphene should be constant with respect to $V_{\text{graphene-Si}}$, which indicated the device diode current. It can be noticed that, at positive $V_{\text{graphene-solution}}$, the amount of I_{Si} and I_{graphene} is identical for all of the cases. This indicates the current is looping inside the closed diode system without transfer of electrons from graphene to the redox states. However, as seen in all of the cases from Figure 3c to Figure 3e, an increase in the measured current, ΔI_{Si} , exists as the $V_{\text{graphene-solution}}$ becomes more negative. This increase in I_{Si} can be explained by either of the mechanisms, (i) a change in the graphene electrode voltage due to the lateral currents on top of the surface and (ii) hydrogen evolution reaction initiated by injected electrons to a graphene/hydrogen complex which directly accepts electrons from the silicon, driving hydrogen generation without the need for a multistep electron transfer without going through any scattering mechanism. Our control experiments analyzing the lateral graphene potential drop (Figure S2) enable us to eliminate the first mechanism. From this, we conclude that the increase in I_{Si} is due to direct injection of electrons from the Si, into graphene, and then immediately transferred from the graphene into the solution before any electron–electron scattering occurs in graphene. This is observable due to the independent voltage control and current measurement of the graphene and silicon terminals. This effect is less prominent as we go to higher $V_{\text{graphene-Si}}$; especially at $V_{\text{graphene-Si}} = 2.0$ V, ΔI_{Si} is almost zero. As stated earlier, increasing $V_{\text{graphene-Si}}$ also increases the energy of the injected electrons. When this energy increases beyond a critical point so that $\Delta E - \lambda - eV_{\text{graphene-solution}} > 0$, electron transfer for these electrons decreases, resulting in a decreased direct injection current. Instead of an increase in ΔI_{Si} , we could observe the amount of solution current increase coming from the change in graphene current, $\Delta I_{\text{graphene}}$. Since these high energy injected electrons cannot directly be transferred to the redox states efficiently, they will scatter within the graphene, eventually giving the energy to the thermal electrons and the lattice. This leads to an increase in the hot electron population and accounts for the increase in I_{graphene} . However, it is important to mention that increasing $V_{\text{graphene-Si}}$ also induces a decrease in the Fermi level of graphene from the Dirac point due to its finite quantum capacitance.^{27,28} An increasingly negative $V_{\text{graphene-solution}}$ has the opposite effect and increases the Fermi level of graphene. These two opposing effects can be explained considering the circuit model shown in Figure S9. The voltage drop in graphene quantum capacitance, C_{Gr} , is manifested as the shift in graphene Fermi level from the Dirac point. Figure S10 shows a heatmap of the Fermi level shift in graphene as a function of both $V_{\text{graphene-Si}}$ and $V_{\text{graphene-solution}}$ for different electrochemical double layer capacitance, C_{DL} , values (1, 50, 100, and 200 $\mu\text{F}/\text{cm}^2$). We consider a range of C_{DL} , as it is expected to increase during the time span of the measurement due to the added pseudocapacitance of the adsorbed hydrogen. Previous investigations on graphene have showed that C_{DL} lies within the range from 1 to 10 $\mu\text{F}/\text{cm}^2$.^{29,30} For such values of C_{DL} , graphene is more likely to be p-doped, as observed in Figure S10. This doped graphene has a different density of thermal electrons compared to undoped graphene, leading to a different thermal current.

To get further insight of this behavior, we have calculated both the direct injected current and hot electron current,

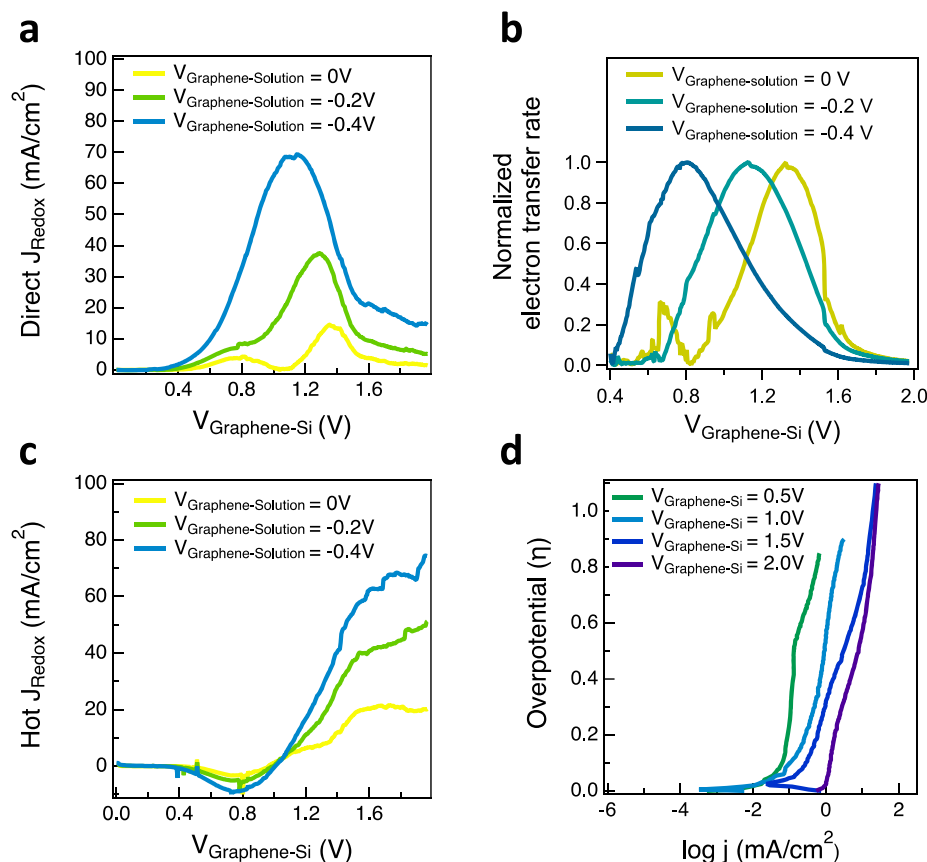


Figure 4. Specific current component extracted from the major current. (a) Direct injection current vs graphene-silicon voltage at different $V_{\text{graphene-solution}}$. (b) Normalized electron transfer rate vs graphene-silicon at different voltages $V_{\text{graphene-solution}}$. (c) Hot electron current vs graphene-silicon voltage at different $V_{\text{graphene-solution}}$. (d) Tafel slopes of different biased probabilities.

which can be extracted from the amount of change in I_{Si} (ΔI_{Si}) and I_{graphene} ($\Delta I_{\text{graphene}}$), respectively, by sweeping the $V_{\text{graphene-Si}}$. Since the direct injection current originates from the unscattered electrons in graphene, it has a very narrow energy distribution that can be approximated to a weighted delta function where the weights are proportional to the diode current, $I_{\text{Gr-Si}}$ and the injection energy is proportional to $V_{\text{graphene-Si}}$. As we change $V_{\text{graphene-solution}}$ from 0 to -0.4 V, we observe direct injection currents to be peaked at certain $V_{\text{graphene-Si}}$ values (Figure 4a). To further understand this behavior, we divide the direct injection current with $I_{\text{Gr-Si}}$ which disentangles the weights of the delta functions and gives us the true distribution of direct injection current as a function of $V_{\text{graphene-Si}}$ and therefore as a function of the energy of the injected electrons. This distribution is a composite of both the electron transfer probability and the tunneling probability of electrons at different injection energies. We call this quantity the electron transfer rate and normalize its maximum to 1 for different $V_{\text{graphene-solution}}$ conditions (Figure 4b). We can clearly observe a Gaussian behavior modulated by non-unity tunneling probability. When we analyze the peaks of the modified Gaussian electron transfer rates shown in Figure 4b, we can observe a negative shift (~ -0.2 V) in these peaks; $V_{\text{graphene-solution}}$ changes by -0.2 V which is consistent with eq 1.

Figure 4c shows the hot electron current extracted from the change of graphene current $\Delta I_{\text{graphene}}$. Hot electrons in this work could be distinguished with the direct injected electrons as electrons which have been scattered inside graphene yet

have higher energy compared to the thermal electrons. However, in this device, the majority of additional solution current occurs due to direct injection. As shown in Figure 4a and c, we can observe the transition of the current components mainly from direct injection electrons to hot electrons. These results coincide with our expectation that the lack of available redox states in the electrolyte limits the amount of direct injection current and increases the hot electron current.

Figure 4d shows the Tafel plots for this device. The most striking feature of this plot is the clear increase in exchange current density as a function of applied $V_{\text{graphene-Si}}$ voltage. Here, we propose that this clear increase as the graphene-silicon voltage is increased follows well with the hot electron model of carrier injection from Si into graphene. Specifically, at higher biases, the electrons injected into the graphene are injected at higher energies, due to the voltage drop across the oxide. This in turn leads to the hot electrons interacting with the solution at a higher energy, which mimics the effect of increasing the temperature of a reaction. However, the exchange current density increases by nearly 2 orders of magnitude, which is unlikely to occur through simple heating of the solution.

To understand the behavior of the hot electrons inside the graphene layer, we have simulated the nonequilibrium electron dynamics using a 2D ensemble Monte Carlo Boltzmann transport equation (MCBTE) solver, as described in the Supporting Information.³¹ Since electrons in graphene are confined in its 2D plane, we can model graphene as a quantum well and calculate how frequently the confined electrons hit the

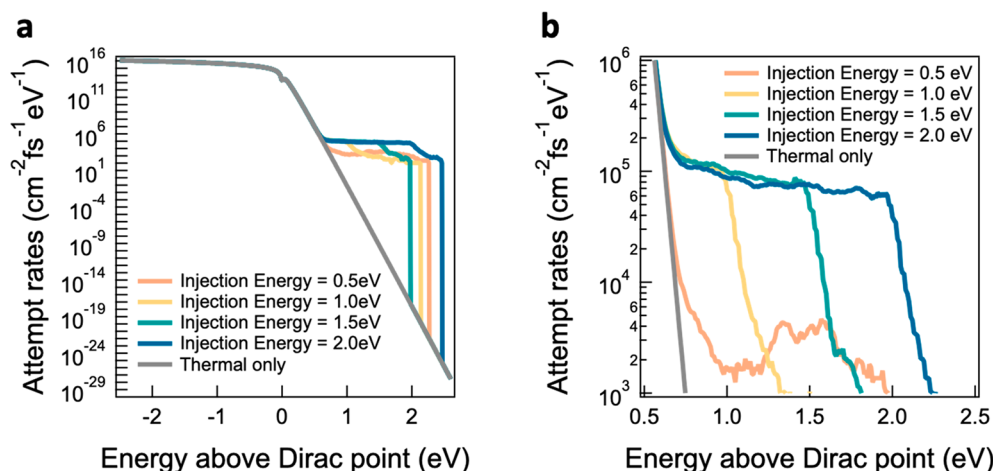


Figure 5. Solving MCBTE for undoped graphene. (a) Attempt rate of electrons tunneling into the graphene/electrolyte junction with 0.5–2.0 eV injection energy above the Dirac point. (b) Zoomed in version of part a at higher electron energies.

energy barriers, i.e., the attempt frequency ($\sim 16 \text{ fs}^{-1}$). Combining this attempt frequency with the electron distributions obtained from the simulations helps us quantify the interaction of graphene electrons with the solution at the graphene–solution interface. Figure 5 shows the energy resolved attempt rates of graphene for injection energies of 0.5–2.0 eV and an injection current of 1 mA/cm^2 for undoped graphene. When there is no injection of hot electrons, the attempt rate profile just follows the graphene density of states and Fermi distribution. However, for a nonzero injection rate, the attempt rates at higher energies are significantly higher compared to the zero-injection situation. Figure 5b shows the attempt rates for higher energy electrons at different injection energies. Here, we see that there is a clear increase in the attempt rate of electrons at higher energies which implies a greater rate of interaction between the high energy electrons and the surface. This increased interaction at higher energies corresponds well to the increase in exchange current density for higher graphene–silicon voltages where the injection energy of electrons is higher.

For an injection current density of 1 mA/cm^2 , we have an injection flux of hot electrons (FHE) = $6.25 \text{ electrons}/(\text{cm}^2 \cdot \text{fs})$. For undoped graphene, an electron injected 1 eV above the Dirac point has an energy loss rate of $\sim 0.1 \text{ eV} \times 10 \text{ ps}^{-1} = 1 \text{ meV/fs}$ for e–e scattering and $\sim 0.2 \text{ eV} \times 50 \text{ ps}^{-1} = 10 \text{ meV/fs}$ for optical phonon scattering.¹⁴ Therefore, the electrons will lose 1 eV energy within $\tau_{\text{HE}} \approx 100 \text{ fs}$. Within this 100 fs, an electron will have the opportunity to interact with the surface, $n_{\text{attempt}} \approx 100 \text{ fs} \times 16 \text{ fs}^{-1} = 1600$ times. This leads to an attempt rate of $\text{FHE} \times n_{\text{attempt}} \approx 6.25 \times 1600 \text{ attempts}/(\text{cm}^2 \cdot \text{fs} \cdot \text{eV}) = 10^4 \text{ attempts}/(\text{cm}^2 \cdot \text{fs} \cdot \text{eV})$. From our simulations, we indeed see an attempt rate of 10^4 – $10^5/(\text{cm}^2 \cdot \text{fs} \cdot \text{eV})$ for electrons injected at 1 eV above the Dirac point for an injection current of 1 mA/cm^2 for undoped graphene.

Figures S6–S9 show the attempt rates for combinations of different injection energies and different doping conditions of graphene. Since p-doped graphene has a very small e–e scattering rate due to its small thermal electron density, the hot electrons do not redistribute their energies with the thermal electrons as effectively and most of their energy decay is due to phonon emission. The injected hot electrons can also gain some energy by absorbing phonons. Due to the lack of redistribution in electron energies, we can observe a peak in

the attempt rates near the injection energy for p-doped graphene, whereas, for undoped and n-doped graphene, the attempt rates monotonically decrease with increasing energy. When a positive voltage is applied between the graphene–silicon junction, graphene starts becoming p-doped as the Fermi level goes down. When the electron is injected into graphene, there is a nonzero probability that it will be transferred directly into the solution before getting back-scattered by the phonons in graphene. The peak observed in the attempt rates near the injection energy means that a major portion of these injected electrons do not go through scattering in p-doped graphene. At the graphene/electrolyte interface, transfer of an electron from graphene to the H^+ ions depends on two important factors: (i) the probability of electrons tunneling through the double layer barrier and (ii) the probability of having a redox state at the same energy due to thermal fluctuation induced broadening. The tunneling probability exponentially increases with the increasing electron energy, and the probability of having a state in the same energy to facilitate the elastic tunneling depends on the applied $V_{\text{graphene-Si}}$ and temperature. The injected electrons that do not face any scattering upon injection have a much higher tunneling probability compared to the thermal electrons. As a result, there is a finite probability that these electrons can directly transfer to the H^+ ions while not bothering the rest of the electrons in graphene. In our experiments, this registers as the direct injection current from silicon to the solution. In a previous work, the same effect was observed for metal electrodes, especially gold. However, for graphene, the direct injection current constitutes a significantly larger portion of the total solution current compared to gold because of this lack of e–e scattering in the p-doped conditions and single layer property.

In conclusion, we demonstrate that a graphene-based SIG diode can act as a source of hot electrons, especially direct injected electrons for efficiently driving electrochemical reductions. By analyzing the individual components, it is possible to not only discover the mechanism of the high energy electron transfer but the characteristic of the graphene/electrolyte junction. A graphene-based hot electron device is not confined to this certain structure; we could possibly get better results by replacing each component with other materials. Future experiments could explore other redox

reactions for carbon dioxide reduction to useful materials and other 2-D materials that transport electrons more efficiently to see if high efficiencies can be achieved at lower voltages.

METHODS

Sample Preparation. Moderately phosphorus doped ($N_d = 5 \times 10^{16} \text{ cm}^{-3}$) (100) silicon wafer (MTI Corporation) was used as the substrate. Native SiO_2 was removed with a 1:10 ratio of $\text{HF}:\text{H}_2\text{O}$ (Sigma-Aldrich, 49% CMOS grade) etching for 1 min. After oxide etching, 1 nm of titanium and 100 nm of silver back contact metals were evaporated in an electron beam evaporator (Temescal, SL1800). To prevent front side damage, a blank Si handle wafer was used after an acetone, IPA, D.I. water rinse. The semiconductor–insulator–graphene (SIG) structure was fabricated by depositing an aluminum oxide insulator layer with atomic layer deposition (Ultratech/Cambridge Savannah ALD) using trimethyl aluminum (Aldrich, 1001278062) and water (Aldrich, W4502) precursors. A single layer of graphene was grown on top of the copper foil by using the chemical vapor deposition (CVD) method by controlling the flow rate of hydrogen (H_2) and methane (CH_4). PMMA (A6495) is spin coated on top of the graphene layer as an adhesion material to transfer the graphene. CVD grown graphene is transferred on top of the aluminum oxide after the copper foil is etched, and PMMA is removed by rinsing with the acetone. For the contact wire attachment, copper wire wrapped with aluminum foil at the one end was used. Two wires are connected to both the front and back sides of the devices each with fast drying silver paint (Ted Pella Inc., 16040-30). A ring contact was drawn in the front side of the device in the graphene layer region. For device encapsulation, a glass slide (VMR Micro slides) was used as a back holder. Fabricated devices with contacts were placed on the glass with epoxy (Gorilla Epoxy clear) to encapsulate the device while leaving the graphene electrode surface exposed.

Electrical Measurements. All of the electrochemical I – V measurements were done by using a potentiostat (Admiral Instrument, Squidstat Prime). Two different channels were used to control separate voltages applied to the system. Each channel has its own working, reference, and counter electrodes. The first channel was connected to the graphene as the working electrode, a platinum wire as the counter electrode, and a Ag/AgCl reference electrode; the second channel consists of a Si emitter as the working electrode, a platinum wire as the counter electrode, and graphene as the reference electrode to bias the graphene–Si junction. 0.5 M H_2SO_4 , 0.1 M KOH, and 1 mM ferrocene with 1 M KCl were used as the electrolyte solution. Dry Schottky and four-probe I – V measurement of devices were characterized by a Semiconductor Parameter Analyzer (Keysight B1500a).

ASSOCIATED CONTENT

Supporting Information

The Supporting Information is available free of charge at <https://pubs.acs.org/doi/10.1021/acs.nanolett.9b05023>.

Additional figures and explanation of simulations (PDF)

AUTHOR INFORMATION

Corresponding Author

Rehan Kapadia – Department of Electrical and Computer Engineering, University of Southern California, Los Angeles,

California 90089, United States; orcid.org/0000-0002-7611-0551; Email: rkapadia@usc.edu

Authors

Hyun Uk Chae – Department of Electrical and Computer Engineering, University of Southern California, Los Angeles, California 90089, United States; orcid.org/0000-0002-7655-2907

Ragib Ahsan – Department of Electrical and Computer Engineering, University of Southern California, Los Angeles, California 90089, United States; orcid.org/0000-0002-3833-7851

Jun Tao – Department of Electrical and Computer Engineering, University of Southern California, Los Angeles, California 90089, United States; orcid.org/0000-0003-2156-1731

Stephen B. Cronin – Department of Electrical and Computer Engineering, University of Southern California, Los Angeles, California 90089, United States; orcid.org/0000-0001-9153-7687

Complete contact information is available at: <https://pubs.acs.org/10.1021/acs.nanolett.9b05023>

Author Contributions

H.U.C., R.A., and R.K. designed the experiments. H.U.C. carried out the sample fabrication and measurements. J.T. carried out graphene growth and ALD. R.A. and R.K. carried out the simulations. H.U.C., R.A., and R.K. contributed to analyzing the data. H.U.C., R.A., and R.K. wrote the paper, while all authors provided feedback. H.U.C. and R.A. contributed equally to this work.

Notes

The authors declare no competing financial interest.

ACKNOWLEDGMENTS

This work was supported by ACS-PRF Grant No. 55993-ND5 (R.K.), AFOSR Grant No. FA9550-16-1-0306 (R.K.), National Science Foundation Award No. 1610604 (R.K.), Army Research Office ARO Award No. W911NF-17-1-0325 (S.B.C.), and the Molecular Foundry at Lawrence Berkeley National Laboratory, a user facility supported by the Office of Science, Office of Basic Energy Sciences of the U.S. Department of Energy (DOE) under Contract No. DEAC02-05CH11231. R.A. acknowledges a USC Provost Graduate Fellowship.

REFERENCES

- Qu, L.; Liu, Y.; Baek, J.-B.; Dai, L. Nitrogen-doped graphene as efficient metal-free electrocatalyst for oxygen reduction in fuel cells. *ACS Nano* **2010**, *4*, 1321–1326.
- Shinagawa, T.; Garcia-Esparza, A. T.; Takanabe, K. Insight on Tafel slopes from a microkinetic analysis of aqueous electrocatalysis for energy conversion. *Sci. Rep.* **2015**, *5*, 13801.
- Mukherjee, S.; Libisch, F.; Large, N.; Neumann, O.; Brown, L. V.; Cheng, J.; Lassiter, J. B.; Carter, E. A.; Nordlander, P.; Halas, N. J. Hot electrons do the impossible: plasmon-induced dissociation of H_2 on Au. *Nano Lett.* **2013**, *13*, 240–247.
- Louidice, A.; Lobaccaro, P.; Kamali, E. A.; Thao, T.; Huang, B. H.; Ager, J. W.; Buonsanti, R. Tailoring copper nanocrystals towards C_2 products in electrochemical CO_2 reduction. *Angew. Chem., Int. Ed.* **2016**, *55*, 5789–5792.
- Tirumala, R. T. A.; Dadgar, A. P.; Mohammadparast, F.; Ramakrishnan, S. B.; Mou, T.; Wang, B.; Andiappan, M. Homogeneous versus heterogeneous catalysis in Cu_2O -nano-

particle-catalyzed C-C coupling reactions. *Green Chem.* **2019**, *21*, 5284–5290.

(6) Lee, H. Y.; Kim, S.; Lee, H. Y. Expansion of active site area and improvement of kinetic reversibility in electrochemical pseudocapacitor electrode. *Electrochem. Solid-State Lett.* **2001**, *4*, A19–A22.

(7) Liu, X.; Sun, L.; Deng, W.-Q. Theoretical Investigation of CO₂ Adsorption and Dissociation on Low Index Surfaces of Transition Metals. *J. Phys. Chem. C* **2018**, *122*, 8306–8314.

(8) Linic, S.; Christopher, P.; Ingram, D. B. Plasmonic-metal nanostructures for efficient conversion of solar to chemical energy. *Nat. Mater.* **2011**, *10*, 911.

(9) Kale, M. J.; Avanesian, T.; Christopher, P. Direct photocatalysis by plasmonic nanostructures. *ACS Catal.* **2014**, *4*, 116–128.

(10) Ge, A.; Videla, P. E.; Rudshiteyn, B.; Liu, Q.; Batista, V. S.; Lian, T. Dopant-Dependent SFG Response of Rhenium CO₂ Reduction Catalysts Chemisorbed on SrTiO₃ (100) Single Crystals. *J. Phys. Chem. C* **2018**, *122*, 13944–13952.

(11) Lee, Y. K.; Choi, H.; Lee, H.; Lee, C.; Choi, J. S.; Choi, C.-G.; Hwang, E.; Park, J. Y. Hot carrier multiplication on graphene/TiO₂ Schottky nanodiodes. *Sci. Rep.* **2016**, *6*, 27549.

(12) Lee, H.; Nedrygailov, I. I.; Lee, Y. K.; Lee, C.; Choi, H.; Choi, J. S.; Choi, C.-G.; Park, J. Y. Graphene-semiconductor catalytic nanodiodes for quantitative detection of hot electrons induced by a chemical reaction. *Nano Lett.* **2016**, *16*, 1650–1656.

(13) Freitag, M.; Steiner, M.; Martin, Y.; Perebeinos, V.; Chen, Z.; Tsang, J. C.; Avouris, P. Energy dissipation in graphene field-effect transistors. *Nano Lett.* **2009**, *9*, 1883–1888.

(14) Rezaeifar, F.; Ahsan, R.; Lin, Q.; Chae, H. U.; Kapadia, R. Hot-electron emission processes in waveguide-integrated graphene. *Nat. Photonics* **2019**, *13*, 843.

(15) Bhimanapati, G. R.; Lin, Z.; Meunier, V.; Jung, Y.; Cha, J.; Das, S.; Xiao, D.; Son, Y.; Strano, M. S.; Cooper, V. R. Recent advances in two-dimensional materials beyond graphene. *ACS Nano* **2015**, *9*, 11509–11539.

(16) Chae, H. U.; Ahsan, R.; Lin, Q.; Sarkar, D.; Rezaeifar, F.; Cronin, S. B.; Kapadia, R. High Quantum Efficiency Hot Electron Electrochemistry. *Nano Lett.* **2019**, *19*, 6227–6234.

(17) Wang, Y. Y.; Ni, Z. H.; Yu, T.; Shen, Z. X.; Wang, H. M.; Wu, Y. H.; Chen, W.; Shen Wee, A. T. Raman studies of monolayer graphene: the substrate effect. *J. Phys. Chem. C* **2008**, *112*, 10637–10640.

(18) Balzani, V. *Electron transfer in chemistry*; Wiley-VCH: Weinheim, Germany, 2001; Vol. 1.

(19) Vanmaekelbergh, D. Electron Transfer at electrodes and Interfaces. *Electron Transfer in Chemistry* **2001**, 126–188.

(20) Muscat, J.; Newns, D. Chemisorption on metals. *Prog. Surf. Sci.* **1978**, *9*, 1–43.

(21) Gerischer, H. Semiconductor electrochemistry. Lawrence Berkeley National Laboratory. LBNL Report #: UCRL-18145, 1968.

(22) Fletcher, S. Tafel slopes from first principles. *J. Solid State Electrochem.* **2009**, *13*, 537–549.

(23) Mukerjee, S. Particle size and structural effects in platinum electrocatalysis. *J. Appl. Electrochem.* **1990**, *20*, 537–548.

(24) Shao, M.; Liu, P.; Zhang, J.; Adzic, R. Origin of enhanced activity in palladium alloy electrocatalysts for oxygen reduction reaction. *J. Phys. Chem. B* **2007**, *111*, 6772–6775.

(25) Laursen, A. B.; Varela, A. S.; Dionigi, F.; Fanchiu, H.; Miller, C.; Trinhammer, O. L.; Rossmeisl, J.; Dahl, S. Electrochemical hydrogen evolution: Sabatier's principle and the volcano plot. *J. Chem. Educ.* **2012**, *89*, 1595–1599.

(26) Zheng, Y.; Jiao, Y.; Li, L. H.; Xing, T.; Chen, Y.; Jaroniec, M.; Qiao, S. Z. Toward design of synergistically active carbon-based catalysts for electrocatalytic hydrogen evolution. *ACS Nano* **2014**, *8*, 5290–5296.

(27) Dröschner, S.; Roulleau, P.; Molitor, F.; Studerus, P.; Stampfer, C.; Ensslin, K.; Ihn, T. Quantum capacitance and density of states of graphene. *Phys. Scr.* **2012**, *2012* (T146), 014009.

(28) Xia, J.; Chen, F.; Li, J.; Tao, N. Measurement of the quantum capacitance of graphene. *Nat. Nanotechnol.* **2009**, *4*, 505.

(29) Shao, Y.; El-Kady, M. F.; Wang, L. J.; Zhang, Q.; Li, Y.; Wang, H.; Mousavi, M. F.; Kaner, R. B. Graphene-based materials for flexible supercapacitors. *Chem. Soc. Rev.* **2015**, *44*, 3639–3665.

(30) Stoller, M. D.; Magnuson, C. W.; Zhu, Y.; Murali, S.; Suk, J. W.; Piner, R.; Ruoff, R. S. Interfacial capacitance of single layer graphene. *Energy Environ. Sci.* **2011**, *4*, 4685–4689.

(31) Sellier, J. M.; Fonseca, J. E.; Klimeck, G. *Archimedes, the free Monte Carlo simulator: A GNU package for submicron semiconductor devices on nanoHUB*, 2012 15th International Workshop on Computational Electronics; IEEE: 2012; pp 1–4.